Journal of Hydrology 517 (2014) 471–480

Contents lists available at ScienceDirect

Journal of Hydrology

journal homepage: www.elsevier.com/locate/jhydrol

Geophysical evaluation of solute plume spatial moments using an adaptive POD algorithm for electrical resistivity imaging

E.K. Oware *, S.M.J. Moysey

Environmental Eng. and Earth Sciences, Clemson University, Brackett Hall, Clemson, SC 29634, United States

ARTICLE INFO

Article history:
Received 5 March 2014
Received in revised form 16 May 2014
Accepted 19 May 2014
Available online 2 June 2014
This manuscript was handled by Peter K. Kitanidis, Editor-in-Chief, with the assistance of Ty Ferre, Associate Editor

Keywords:
Spatial moments
Resistivity imaging
Proper Orthogonal Decomposition
Physics-based regularization
Model Order Reduction

SUMMARY

We investigate the potential for characterizing spatial moments of subsurface solute plumes from surface-based electrical resistivity images produced within a Proper Orthogonal Decomposition (POD) inversion framework. The existing POD algorithm is improved here to allow for adaptive conditioning of the POD training images on resistivity measurements. The efficacy of the suggested technique is evaluated with two hypothetical transport scenarios: synthetic #1 is based on the case where the target plume and POD training images follow the same (unimodal) plume morphology, whereas a second source location in synthetic #2 makes the target plume bimodal and inconsistent with the POD training images. The resistivity imaging results indicate that the adaptive algorithm efficiently and robustly updates the POD training images to obtain good quality resistivity images of the target plumes, both in the presence of data noise and when conceptual model inaccuracies exist in the training simulations. Spatial moments of the solute plumes recovered from the resistivity images are also favorable, with relative mass recovery errors in the range of 0.6–4.4%, center of mass errors in the range of 0.6–9.6%, and spatial variance errors in the range of 3.4–45% for cases where the voltage data had 0–10% noise. These results are consistent with or improved upon those reported in the literature. Comparison of the resistivity-based moment estimates to those obtained from direct concentration sampling suggests that for cases with good quality resistivity data (i.e., <3% noise), the imaging results provide more accurate moments until 6–10 multilevel sampling wells are installed. While the specific number of wells will depend on the actual field scenario, we suggest that this finding illustrates the general value of POD-based resistivity imaging techniques for non-invasively estimating the spatial moments of a solute plume.

Published by Elsevier B.V.

1. Introduction

Hydrogeologists often employ statistical moments to describe the morphology of subsurface solute plumes and provide valuable insights to the spatiotemporal evolution of transport processes (e.g., Freyberg, 1986; Goltz and Roberts, 1987; Yeh et al., 2005). Spatial moments play a vital role in numerous hydrological applications such as the design of ground-water quality monitoring networks (e.g., Loaiciga et al., 1992), characterization of flow regimes (e.g., Ye et al., 2005; Yeh et al., 2005; Lazarovitch et al., 2007; Xiong et al., 2011), and the analysis of solute plume behavior (Brewster et al., 1995; Rubin, 2003; Fernàndez-Garcia et al., 2005; de Barros and Nowak, 2010). The two-dimensional spatial moments, $m_{i,j}$, for the image of a solute plume with concentrations $\mathbf{c}(x_k, y_k)$ at locations x_k and y_k can be expressed as:

$$m_{i,j} = \sum_{k}^{NxM} \mathbf{c}(x_k, y_k) x_k^i y_k^j \Delta x \Delta y, \tag{1}$$

where $m_{i,j}$ represents the spatial moment of interest and the overall order of the moment is defined by the sum $i+j$. Here k represents the element index in a discretized representation of the subsurface, Δx and Δy are the dimensions of the pixels, and it is assumed that background concentration variations unrelated to the plume have been removed. The zero-order moment, $m_{0,0}$, quantifies the total mass in the system. The x and y coordinates of the center of mass of the plume can be inferred from the first-order moments ($m_{1,0}$ and $m_{0,1}$):

$$\mu_x = m_{1,0}/m_{0,0},$$
$$\mu_y = m_{0,1}/m_{0,0}.$$

Similarly, the longitudinal and transverse dispersive spreading of the plume can be evaluated from the second-order moments ($m_{2,0}$, $m_{0,2}$, and $m_{1,1}$):

* Corresponding author. Tel.: +1 309 532 4075.
E-mail address: eoware@clemson.edu (E.K. Oware).

http://dx.doi.org/10.1016/j.jhydrol.2014.05.054
0022-1694/Published by Elsevier B.V.

$$\sigma_x = \sqrt{\frac{m_{2,0}}{m_{0,0}} - \left(\frac{m_{1,0}}{m_{0,0}}\right)^2},$$

$$\sigma_y = \sqrt{\frac{m_{0,2}}{m_{0,0}} - \left(\frac{m_{0,1}}{m_{0,0}}\right)^2}.$$

Conventional direct-sampling of concentration approaches (e.g., Everett, 1980; Freyberg, 1986; LeBlanc et al., 1991) are typically applied to gain insight into the spatial extent of subsurface solute plumes. Direct sampling of concentrations, however, is invasive, expensive, and introduces contaminant mobilization risks. In contrast, geophysical methods have the potential to noninvasively estimate spatial moments of conductive solute plumes with low costs and minimal risk.

In a 2-D hypothetical example, for instance, Pidlisecky et al. (2011) formulated a distribution-based parameterization inversion framework from which they successfully characterized spatial moments of plumes from cross-borehole radar tomograms. In a field-scale application, Binley et al. (2002) accurately retrieved spatial moments of fluid flow in the vadose zone using electrical resistivity tomography (ERT). Singha and Gorelick (2005) and Müller et al. (2010) used spatial moments from time-lapse ERT images to investigate transport processes. Hubbard et al. (2001) went further by utilizing spatial moments derived from ERT images to calibrate aquifer flow and transport parameters.

Some challenges regarding the accuracy of moments estimated from geophysical tomograms, such as underestimation of mass and smearing of plumes, have been reported as a result of imaging artifacts (e.g., Singha and Gorelick, 2005; Day-Lewis et al., 2007). To investigate the drawbacks associated with resolving moments from geophysical tomograms, Day-Lewis et al. (2007) derived a semi-analytical moment-resolution matrix. The authors used this tool to conclude that the geophysically recovered plume moments are dependent on the measurement sensitivity, survey geometry, regularization criteria, and measurement errors.

One particularly important cause of tomographic errors has been attributed to limited choices for regularization criteria needed to stabilize the mathematics of the imaging problem (e.g., Oware et al., 2013). Commonly utilized regularization constraints are based on deviations from a reference value or the minimization of the first and second spatial derivatives, which respectively invoke smallness, flatness, and smoothness in the recovered solution (Tikhonov and Arsenin, 1977; Pidlisecky et al., 2007). While these constraints are often considered "objective" choices, they may not be optimal for representing how the physics of the underlying process, e.g., groundwater flow and transport, produce spatial property variations, i.e., plume concentrations.

Oware et al. (2013) introduced a Proper Orthogonal Decomposition (POD) constrained inversion strategy to leverage site-specific, physics-based *a priori* information to constrain geophysical inverse problems in a flexible fashion by invoking soft process constraints. The technique applies POD (e.g., Banks et al., 2000; Kunisch and Volkwein, 2003; Rathinam and Petzold, 2004; Pinnau, 2008) to obtain a physics-based POD basis, i.e., set of vectors representing process-relevant spatial patterns, from site-specific Training Images (TI). The basis patterns are subsequently utilized to constrain the inversion procedure. The TIs are generated using Monte Carlo simulations to mimic the perceived physical mechanisms of interest, which in this study are conservative groundwater flow and transport in heterogeneous aquifers.

The POD algorithm is a model order reduction (MOR) technique since it maps a high-order dimensional state-space into a low-order dimensional coefficient-space via optimally selected basis functions. The geophysical optimization then proceeds in the low-order dimensional coefficient-space resulting in the estimation of fewer inversion parameters compared to the original dimensionality of the problem. While MOR techniques are extensively researched in other scientific and engineering disciplines such as applied mathematics (e.g., Li et al., 2009; Yao and Meerbergen, 2013) and image processing (e.g., Milanfer et al., 1996), the technique remains largely under-explored in the field of hydrogeophysics. In contrast to our use of POD as a sparse basis for representing the parameter space, the use of POD in groundwater inverse problems generally tends to focus on improving the computational efficiency of the forward model (e.g., Winton et al., 2011).

In the context of solute plume imaging, available literature related to MOR mainly employs optimal parameterization of the state-space based on statistical moments (e.g., Pidlisecky et al., 2011) or object-based-inversion (OBI) (e.g., Miller et al., 2000; Lane et al. 2004, 2006) that seeks to reduce the number of inversion parameters required to fully describe the target plume, while simultaneously invoking *a priori* constraints regarding the physics or geometry of the target features. In contrast to these approaches POD is a MOR technique that can directly leverage advances in mechanistic modeling in an effort to capture and incorporate realistic, non-parametric, site-specific hydrological process patterns into hydrogeophysical inversion schemes.

A problem with the proposed POD-based inversion scheme, however, was that it lacked the ability to shift basis patterns in space. Hence, the center of mass of the TIs had to be positioned in close proximity to the true center of mass for the plume being imaged. Oware et al. (2013) assumed that the center of mass could be approximated prior to the detailed reconstruction of a resistivity image using methods similar to Pidlisecky et al.'s (2011) distributed parameterization or Fowler and Moysey's (2011) coupled inversion approach, where resistivity data were used to calibrate the effective properties of an analytical transport model. The dependence of the POD approach on this assumption is a major limitation of the algorithm as initially proposed by Oware et al. (2013).

The objective of this paper is twofold. First, we address the limitations of the original POD imaging method to adaptively estimate the solute plume center of mass within the POD-constrained imaging algorithm. We hypothesize that the plume's true center of mass can be evaluated by recursively reconstructing resistivity images as the center of mass of the POD training images is successively updated in each iteration, thereby adaptively conditioning the center of mass to the resistivity data. Second, we evaluate the accuracy of solute plume spatial moments derived from POD-based images using two synthetic transport experiments.

In this paper, we present the proposed adaptive POD-constrained inversion algorithm in Section 2. Details of the numerical experiment used to test the efficacy of the suggested scheme are then provided in Section 3. Results of the investigation including the impact of resistivity measurement errors on the POD-based spatial moments, and comparison to moments estimated by direct sampling from multi-level wells are outlined in Section 4. Section 5 summarizes the key conclusions of the study.

2. Adaptive algorithm for POD-constrained Imaging

The working details of traditional ERT are extensively documented in the literature (e.g., Kemna et al., 2002). The standard protocol for ERT surveys involves the successive application of electric current (I) to the subsurface via electrodes deployed in the ground. The current flow induces voltages ($\mathbf{V}_{obs}$) dependent on the spatial distribution of electrical resistivity (inverse of electrical conductivity, $\boldsymbol{\sigma}$), which is controlled by the physical properties of the earth (e.g., solute concentrations). The observed voltages are subsequently utilized to reconstruct the electrical conductivity

distributions. POD inversion described by Oware et al. (2013) is a variant of Tikhonov regularization that employs a physics-based *a priori* model to constrain the optimization procedure.

The POD inversion represents subsurface conductivities as a linear combination of M basis vectors, i.e.,

$$\boldsymbol{\sigma} = \mathbf{Bc}, \tag{2}$$

where the columns of the set $\mathbf{B} \in \mathbf{R}^{MxM}$ represent the basis vectors that capture spatial patterns relevant to the imaging problem. The rows of the expansion coefficient $\mathbf{c} \in \mathbf{R}^{Mx1}$ denote the magnitude of components of $\boldsymbol{\sigma}$ in the basis space (i.e., projected within the POD coordinate system). Implementing Eq. (2) within the traditional Tikhonov regularization (Tikhonov and Arsenin, 1977), the objective function for POD-constrained inversion can be defined as:

$$\begin{aligned}\mathbf{E}(\mathbf{c}) &= \mathbf{E}_d + \beta \mathbf{E}_m = \|\mathbf{W}_d[\mathbf{V}_{obs} - \boldsymbol{f}_g(\mathbf{Bc})]\|_2 + \beta \mathbf{W}(\mathbf{Bc} - \mathbf{Bc}_0\|_2 \\ &= \|\mathbf{W}_d[\mathbf{V}_{obs} - \boldsymbol{f}_g^*(\mathbf{c})]_2 + \beta \|\tilde{\mathbf{W}}(\mathbf{c} - \mathbf{c}_0\|_2\end{aligned} \tag{3}$$

The $\mathbf{E}_d$ term is the data norm, which measures the fit between observed and modeled data, whereas $\mathbf{E}_m$ is the model norm, which introduces prior information about $\boldsymbol{\sigma}$. The data weighting matrix, $\mathbf{W}_d$, is a diagonal matrix containing the inverse of the standard deviations of the measured data along its diagonal. In this study, $\mathbf{W}_d$ is formulated according to Pidlisecky et al. (2007). The regularization parameter, β is utilized to tune the relative importance of data fit versus model regularization. Additionally, $f_g^*(\cdot)$ denotes a transformed resistivity forward model functional that incorporates the reconstruction of $\boldsymbol{\sigma}$ from the POD basis. The regularization operator, $\mathbf{W}$ contains information that enforces spatial criteria (e.g., flatness and continuity) within the reconstructed images. Notice that while the regularization operator, $\mathbf{W}$ acts in the original model space, the composite regularization filter $\tilde{\mathbf{W}}$ acts in the transformed coefficient ($\mathbf{c}$) domain and is described in detail later. The reference conductivity model is denoted by $\boldsymbol{\sigma}_0$ or equivalently $\mathbf{c}_0 = \mathbf{B}^T\boldsymbol{\sigma}_0$.

The conceptual algorithm for Oware et al.'s (2013) original POD-constrained inversion is outlined in Fig. 1. The overall implementation proceeds in four major steps, namely: (i) Monte Carlo simulation of TIs that capture the influence of the target process on state variables, (ii) construction of POD basis (B), (iii) optimization of expansion coefficients (c), (iv) reconstruction of *in situ* target profiles ($\boldsymbol{\sigma}$). Note that if the retrieved model is found to be inconsistent with the assumptions underlying the generation of the training dataset, the initial process hypotheses can be reconceptualized, e.g., based on the imaging results, and the entire data inversion process repeated in the same fashion for improved estimation. The POD approach can therefore also aid in conceptual model development.

In the construction of the POD-bases, the rows of the training dataset, $\mathbf{D} \in \mathbf{R}^{NxM}$, contain the N realizations of the simulated TIs, $\boldsymbol{\sigma}^{TI} \in \mathbf{R}^{1xM}$, obtained by Monte Carlo simulation of relevant flow and transport processes. The POD basis vectors can be approximated from $\mathbf{D}$ in a least-square minimization manner (e.g., Kunisch and Volkwein, 2003; Pinnau, 2008), or via Singular Value Decomposition (SVD) (e.g., Castleman, 1996). Using SVD, the training dataset can be factorized into its respective left and right singular vectors $\mathbf{U}$ and $\mathbf{V}$, along with their corresponding singular values $\boldsymbol{\Lambda}$:

$$\mathbf{D} = \mathbf{U}\boldsymbol{\Lambda}\mathbf{V}^T, \tag{4}$$

where $\mathbf{U} \in \mathbf{R}^{NxN}$, $\mathbf{V} \in \mathbf{R}^{MxM}$ and $\boldsymbol{\Lambda} \in \mathbf{R}^{NxM}$. In practice, the spatial patterns most characteristic of the TIs are captured by the first p basis vectors where $p \ll M$, such that $\mathbf{V}$ can be truncated without introducing significant reconstruction errors (Oware et al., 2013). The truncation criterion is based on a user-defined threshold of percentage contribution of singular values of the p selected basis vectors with respect to the overall M singular values weight. There are situations, however, where a single basis vector can account for over 99% of the overall variability in the training data. In this case, the above specified truncation criterion will fail to include high-order basis patterns vital to reconstructing details in the geometry of the target plume.

To address this challenge, we suggest an alternative truncation criterion based on imaging error. In this approach, an arbitrary

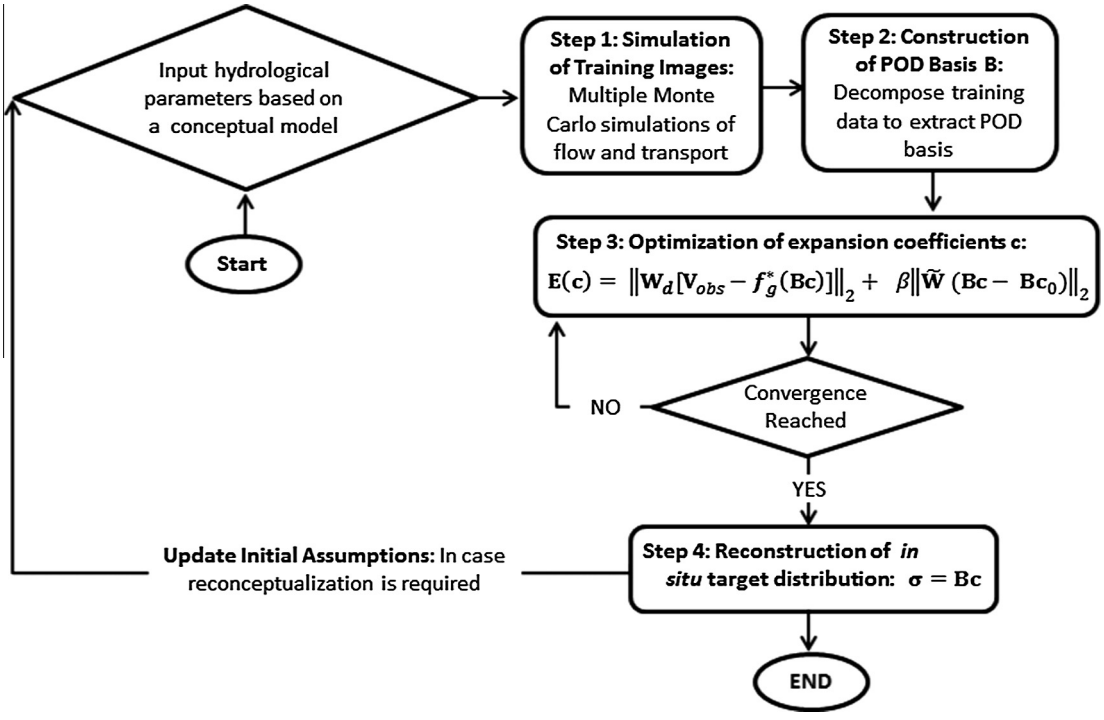

Fig. 1. Schematic illustration of the conceptual algorithm for the implementation of the POD-constrained inversion.

hypothetical plume model is projected into the coefficient space and then reconstructed based on varying numbers (p) of basis functions. The error of the reconstructed image can then be estimated as a function of p to identify an acceptable truncation. For this exercise, we suggest applying a more complicated hypothetical plume as compared to the TIs used in generating the basis library to avoid truncation of important high-order patterns. Illustrative examples of POD basis functions used in this study are shown in Fig. 2.

The formulation of the regularization filter, $\mathbf{W}$, in the Cartesian model space is a combination of difference operators as suggested by Ellis and Oldenburg (1994):

$$\mathbf{W}^T\mathbf{W} = \mathbf{gx}_2^T\mathbf{gx}_2 + \mathbf{gy}_2^T\mathbf{gy}_2 + \delta\mathbf{M}_w^T\mathbf{M}_w,$$

where $\mathbf{gx}_2$ and $\mathbf{gy}_2$ represent the discretized lateral and vertical second derivative spatial filters, respectively, which penalize for roughness in the spatial distribution of the model parameters. $\mathbf{M}_w$ denotes the model weights matrix, which penalizes against the propagation of singular errors near the electrodes (e.g., Fox, 1979; Dey and Morrison, 1979). The smallness factor, δ, is a fitting parameter that is utilized to tune the relative importance of these penalties. The filter $\mathbf{W}$ is projected into the coefficient space as

$$\tilde{\mathbf{W}}^T\tilde{\mathbf{W}} = \mathbf{B}^T\mathbf{W}^T\mathbf{W}\mathbf{B} + \lambda\mathbf{W}_{sv}, \quad (5)$$

while introducing additional constraints $\mathbf{W}_{sv}$ based on the singular values of the training dataset $\mathbf{D}$. The singular values represents the variance (or importance) of the basis vectors in the POD coordinate system for capturing the training data, therefore, $\mathbf{W}_{sv}$ imposes an *a priori* structural constraint on the optimization procedure that biases the images toward the TIs. Another fitting parameter, λ, is applied to balance out the relative importance of the conventional regularization constraints versus the TIs.

Following the generation of site-specific, non-parametric POD bases and the optimization of the transform coefficients, $\mathbf{c}$, the *in situ* electrical conductivity distributions can be approximated via Eq. (2) (step 4 in Fig. 1).

The POD technique as described above is unable to shift the location of the basis vectors toward the location of the true plume during the optimization procedure. The method therefore requires that the TIs can be located in the vicinity of the true plume prior to initiating image reconstruction. To overcome this limitation, we propose a simple strategy to adaptively estimate the center of mass of the solute plume within the POD inversion scheme from surface-based resistivity measurements.

The adaptive POD algorithm is heuristically illustrated in Fig. 3. First, an initial estimate of the center of mass of the true plume is used to position the training images (or equivalently the POD basis); note that this location must be within the region of sensitivity of the resistivity measurements though it need not be in the immediate vicinity of the actual plume being imaged. The standard POD algorithm (Fig. 1) is then used to obtain an estimate of the resistivity image. After the data inversion, the center of mass of the retrieved tomogram is estimated and used to reposition the Tis (or POD basis vectors) for the next iteration. This process is repeated until convergence is reached, where we define the convergence criterion based on a data-fit tolerance limit.

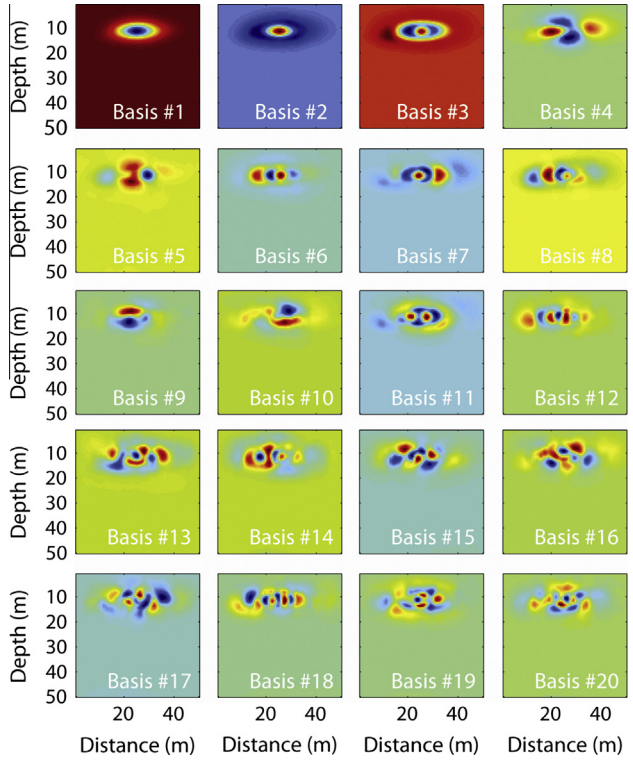

Fig. 2. Illustrative examples of the first 20 dominant basis patterns extracted from the decomposition of the training images.

3. Methods

Two hypothetical transport experiments were applied to test the proposed strategy and evaluate the accuracy of the resulting plume moments. A schematic illustration of the experimental setup is provided in Fig. 4. The simulations resulted in two synthetic targets, synthetic #1 and synthetic #2 (Figs. 5a and 6a), Both examples assume conservative solute transport through a two dimensional, heterogeneous cross section of the subsurface in response to a horizontally applied uniform hydraulic gradient. The top and bottom boundaries of the system represent zero flux conditions. Resistivity surveys are collected using electrodes placed near the top of the model domain, i.e., at the ground surface. The difference between the two scenarios is that synthetic #1 contains a single source for the solute, thereby producing a unimodal plume, whereas synthetic #2 contains an additional solute source, leading to a bimodal solute plume. Archie's law (Archie, 1942) was used for both the forward and inverse transformation of concentration to electrical conductivity. We therefore do not explicitly account for petrophysical scaling effects as discussed in previous work by Moysey and Knight (2004), Moysey et al., 2005 and Singha and Moysey (2006). Refer to Oware et al. (2013) for further specific details of the hydrological simulations for the test examples and the training images, and also the details of the resistivity survey and the ERI inversions.

The conceptual algorithm for the estimation of the plume center of mass (Fig. 3) requires the selection of an initial location for the POD basis vectors. To explore the impact on the quantification of the true center of mass as a result of the anisotropic nature of resistivity sensitivities (e.g., Keller and Frischknecht, 1966), three scenarios were investigated where the initial position was laterally, vertically, or diagonally shifted relative to the true center of mass.

To control the positioning error, the initial center of mass was shifted in proportion to the true plume's width as described by the lateral and vertical second spatial moments (e.g., Freyberg, 1986; Goltz and Roberts, 1987). While the lateral perturbation of the x-coordinate was 16 m, the y-coordinate was vertically shifted by 9 m. For instance, for a true center of mass of (x_0, y_0), the vertical, lateral, and diagonal positioning errors were $(x_0,\ y_0 + 9)$, $(x_0 + 16,\ y_0)$, $(x_0 + 16,\ y_0 + 9)$, respectively. To provide a constant basis for comparing all the results, these positioning errors were kept constant for all the data inversions.

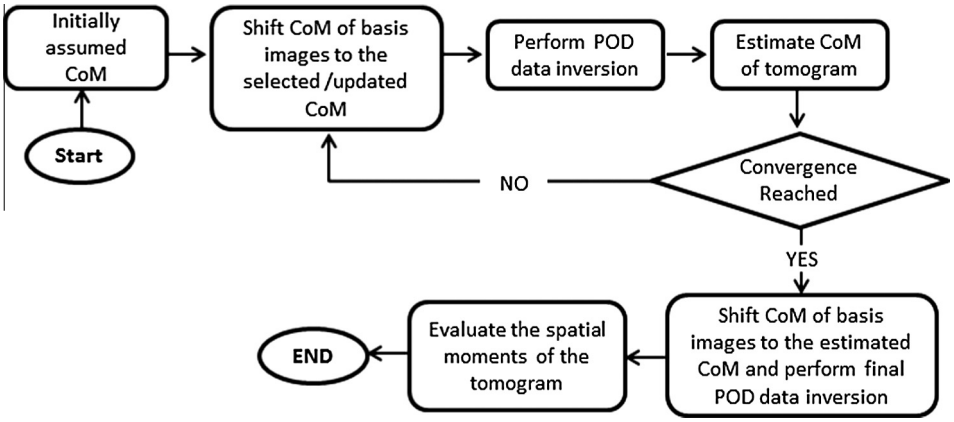

Fig. 3. Conceptual algorithm to estimate the spatial moments of a targeted subsurface distribution from resistivity measurements. CoM refers to center of mass.

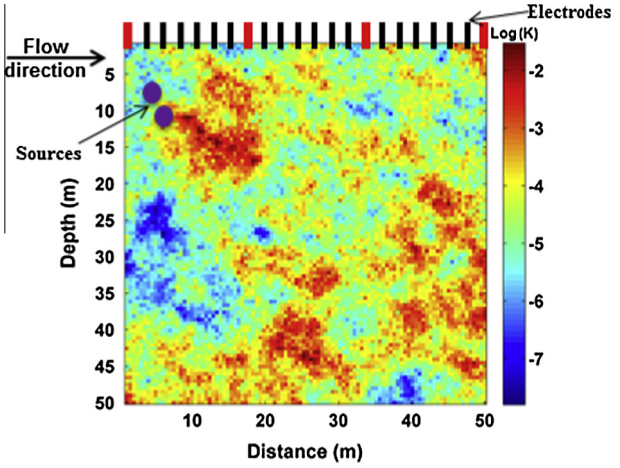

Fig. 4. Schematic illustration of the experimental setup of the 2-D flow and transport in a random hydraulic conductivity field (image color scale denotes the value of the log of K). The design of the resistivity surveys illustrated by the electrodes along the ground (top) surface; while the red electrodes served as both current and potential electrodes, the black electrodes were used exclusively as potential electrodes leading to a total of 120 resistance measurements in each survey. (For interpretation of the references to color in this figure legend, the reader is referred to the web version of this article.)

Furthermore, in an effort to explore how data uncertainties affect the predictive power of the center of mass, we assumed random Gaussian errors with standard deviations proportional to the resistivity signals, according to the following noise model:

$$\mathbf{d}_{noise} = \mathbf{d}_{no\_noise} + n_{per} \cdot \mathbf{d}_{no_{noise}} \cdot \mathrm{N}(0,1), \tag{6}$$

where $\mathbf{d}_{noise}$ and $\mathbf{d}_{no\_noise}$ represent the corrupted and noise-free data, respectively. n_{per} denotes the proportion of the resistivity signal to be added as noise. In this study, we investigated scenarios where n_{per} was set to 0, 0.03 (3%), and 0.1 (10%). N(0, 1) signifies a random normal distribution with zero mean and standard deviation of one. While assuming simple Gaussian noise model may be adequate for our demonstrations here, empirical errors in applications can be estimated based on reciprocal measurements (interchanging injection and receiver electrodes) as presented by LaBreque et al. (1996). To evaluate the influence of noise on the center of mass estimation, the data inversion was performed for 100 datasets generated from the excitation of $\mathbf{d}_{no\_noise}$ with 100 realizations of Gaussian noise.

4. Results and discussion

4.1. Estimation of electrical conductivity images

Estimated conductivity images of the plume obtained for each iteration of the adaptive POD inversion are shown in Figs. 5 and 6 for synthetic #1 and synthetic #2, respectively; these results represent the case where the POD TIs were initially laterally displaced from the true center of mass by 16 m. Note that the assumed center of mass used to position the POD TIs is shown as white star in these images, which moved progressively toward the true plume center of mass (shown as white cross) as the inversion proceeds. Results are presented for cases where 0%, 3%, and 10% errors were added to the voltage measurements prior to the inversion.

As the adaptive POD inversion progresses for synthetic #1, the images in Fig. 5 consistently improve as the TIs are shifted toward the true location of the plume. The influence of noise is qualitatively apparent in the images as over fitting of the data errors causes spurious non-zero conductivities to appear in the regions away from the true plume, which is spatially compact. This observation is quantitatively supported by a consistent increase in the root mean square error (RMSE) of the estimated plume concentration with increasing noise (Table 1). It is also apparent, however, that noisy data requires more iterations for the algorithm to converge toward an acceptable image of the true plume.

The situation is somewhat different for synthetic #2, where the estimated images significantly degrade in early iterations before finally converging toward an acceptable solution (Fig. 6b–j). In this case, the adaptive POD algorithm also requires substantially more iterations to converge for the zero noise case compared to the cases with noise added (Fig. 6), though the RMSE of the final concentration estimates is ultimately superior for the noise-free case (Table 1). The difference in behavior compared to synthetic #1 is due to the fact that the model used to generate the POD TIs, i.e., a unimodal plume with a single source zone, is inconsistent with the actual solute plume being imaged in synthetic #2, i.e., a bimodal plume generated by releases from two distinct source zones. The inconsistency between the *a priori* conceptual model of the system built into the POD basis versus the resistivity measurements that are representative of the actual plume makes it more difficult for the algorithm to efficiently converge toward an acceptable solution. The data noise stabilizes the inversion, but at the same time causes a loss of resolution in the final estimated images.

The results in Figs. 5 and 6 represent the case where the POD TIs were shifted laterally away from the true center of mass of the plume. In Fig. 7 we evaluate the sensitivity of the adaptive

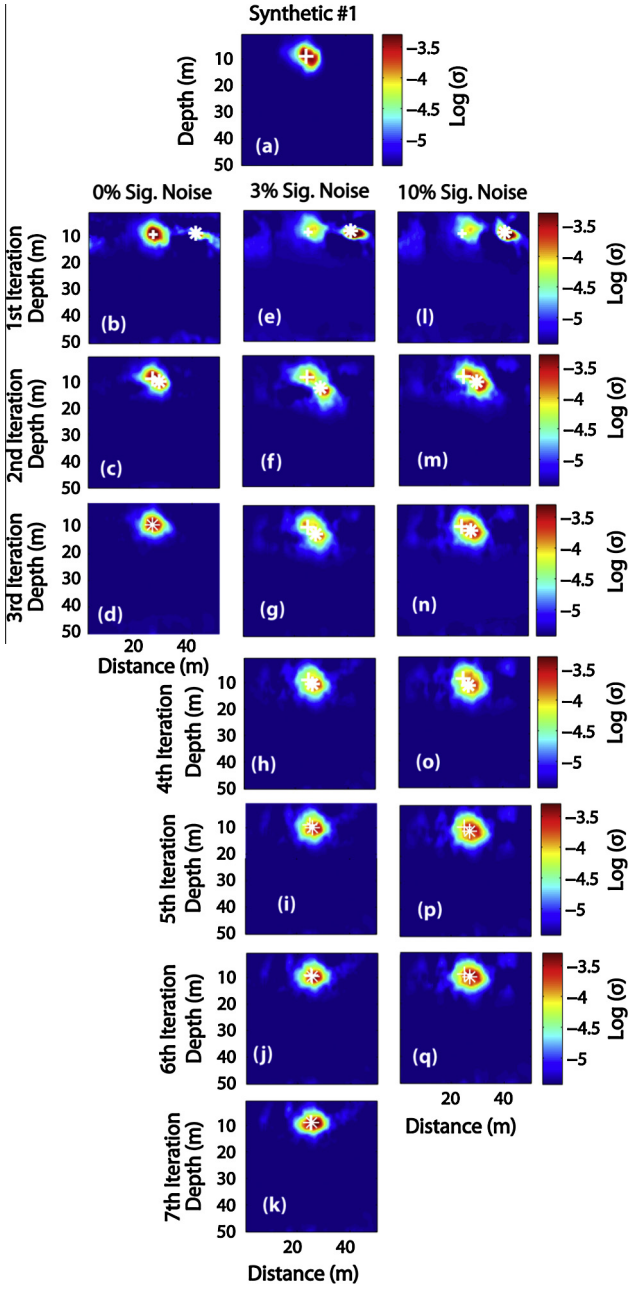

Fig. 5. Log of electrical conductivity tomograms demonstrating the iterative reconstructions to estimate center of mass from resistivity measurements for the case of lateral shift of the true center of mass. Synthetic #1 (a). Tomograms showing successive reconstructions from the first to the converged iterations for: 0% data noise (b–d, column 1), 3% noise (e–-k, column 2) and, 10% noise perturbation (i–q, column 3). The white + in each image denotes the position of the center of mass of the true plume, whereas the white * indicates the location of the center of mass of the training dataset for that iteration. Note, it seems the location of the white * gets closer to the white + with each update, in most cases.

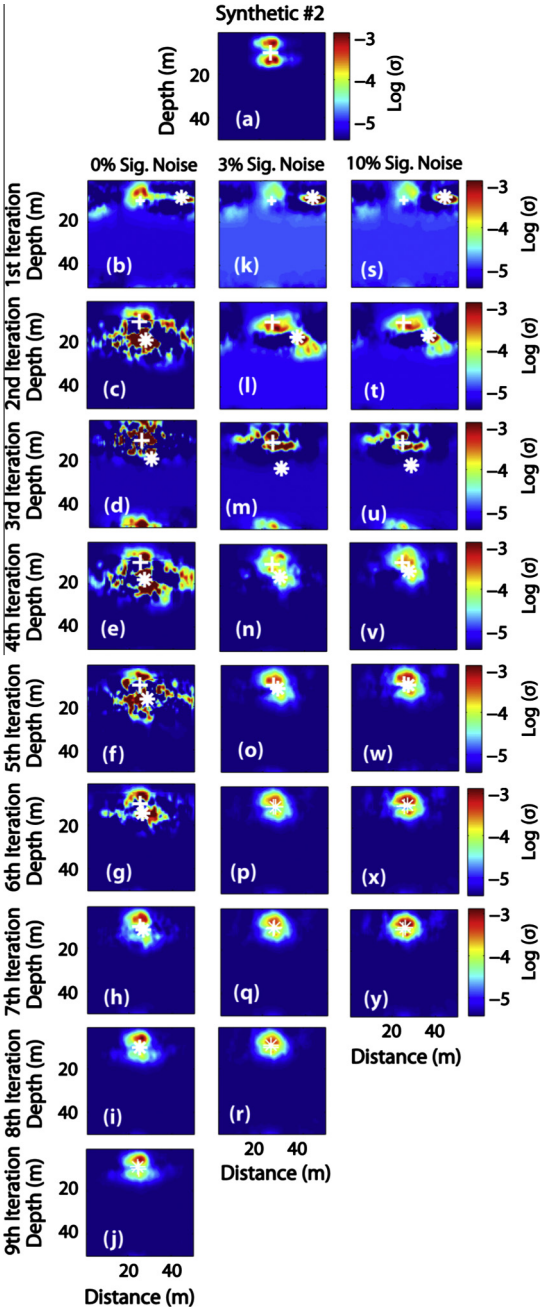

Fig. 6. Log of electrical conductivity tomograms demonstrating the iterative reconstructions to estimate center of mass from resistivity measurements, for the example of lateral positioning error. Synthetic #2 (a). Tomograms showing successive reconstructions from the first to the converged iterations for: 0% data noise (b–j, column 1), 3% noise (k–r, column 2) and, 10% noise perturbation (s–y, column 3). The white + in each image denotes the position of the center of mass of the true plume, whereas the white * indicates the location of the center of mass of the training dataset for that iteration. Note, it appears location of the white * gets closer to the white + with each update, in most cases.

inversion to the direction in which the POD TIs are initially shifted relative to the true plume center of mass (i.e., lateral, vertical, or diagonal). After each tomographic update the refined location of the TIs approaches the true center of mass of the plume, regardless of the direction in which the TIs were originally perturbed (Fig. 7). This continuous improvement reflects improved utilization of the resistivity data within the inversion to incorporate information about the true plume while decreasing the dependence on the assumed *a priori* transport model. This observation is consistent with the underlying hypothesis of this study.

It is notable that the location of the training images converged to the same position regardless of the initial displacement direction for the TIs. This observation suggests that the adaptive POD algorithm is insensitive to errors in TI positioning (though TIs must be located within a region of sensitivity to the resistivity measurements). In contrast, it is also apparent that as noise is added to the measurements, the converged location of the TIs relative to the true center of mass deteriorates. This observation suggests that the inversion approach is sensitive to data noise.

Table 1
True and calculated spatial moments for the final concentration estimates obtained for scenarios with 0%, 3%, and 10% signal noise in the resistivity data.

Noise additive (%)	Total mass (kg)	Center of mass (m)		Variance (m^2)	
		μ_x	μ_z	σ_x^2	σ_z^2
Synthetic #1					
True values	1.58	25.06	8.55	8.66	7.09
0	1.59	24.80	8.42	8.35	6.85
3	1.59	25.22	8.44	9.50	5.54
10	1.65	26.32	9.37	11.48	8.46
Synthetic #2					
True values	1.75	24.87	9.44	12.92	17.77
0	1.70	24.75	10.29	14.56	15.16
3	1.71	25.02	9.95	14.43	11.29
10	1.77	25.86	9.08	13.53	9.77

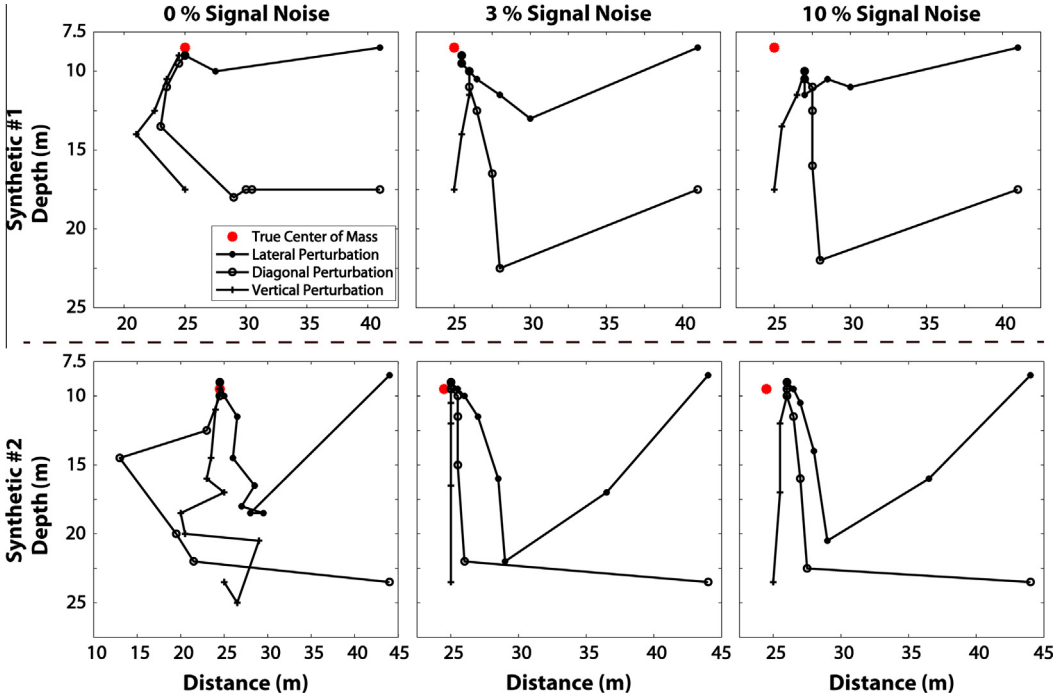

Fig. 7. Plots showing the update paths for the position of the POD training images: synthetic #1 (row 1), synthetic #2 (row 2). Red circles signify true CoM, black filled circles represent initial lateral shifts in the training image positions, whereas black open circles indicate diagonal shifts and plus symbols denote vertical shifts. Columns 1–3 represent 0%, 3%, and 10% signal noise additives, respectively. Observe that for each noise case studied, the estimation of the center of mass from all the perturbed directions, converged at a unique location. (For interpretation of the references to color in this figure legend, the reader is referred to the web version of this article.)

To investigate the influence of data noise on the adaptive updating of the TI positions we generated 100 realizations of Gaussian noise to corrupt the voltage measurements and subsequently performed an independent adaptive POD inversion for each corrupted data set. Fig. 8 shows the mean and standard deviation for the final converged location of the TIs performed with the set of 100 noisy datasets. As the data noise increases, there are two clear impacts on how the TI positions are updated in the adaptive algorithm: (1) on average the position of the TIs converges farther away from the true center of mass of the plume, i.e., there is greater positioning error for the final image reconstruction step in the adaptive algorithm; and (2) there is substantially greater spread in the final converged position of the TIs for the cases with higher data errors. Both of these results suggest that the resistivity data contain less information to constrain the adaptive algorithm as the noise level increases, which is consistent with the degradation of the plume concentration estimates indicated by the RMSE values in Table 1 and the general loss of performance of tomographic imaging techniques with noisy data.

The final positioning errors appear to be minimized when starting the TIs with a vertical displacement relative to the true plume compared to lateral and diagonal shifts for both the 3% and 10% noise cases. This observation, however, may be related to the specifics of the morphology and position of the true plume relative to the sensitivity pattern of the resistivity survey or the fact that the TIs were shifted proportionally to the concentration plume moments, thus the original TI displacement was effectively smaller in the vertical than the lateral or diagonal directions. Of greater concern, however, is an apparent systematic bias in the final position of the training images relative to the true plume regardless of how the TIs are initially perturbed. Given that the training images capture patterns associated with the *a priori* model of transport, this bias could also be related to an inconsistency between the morphology of the TIs and the true plume. The potential significance of the

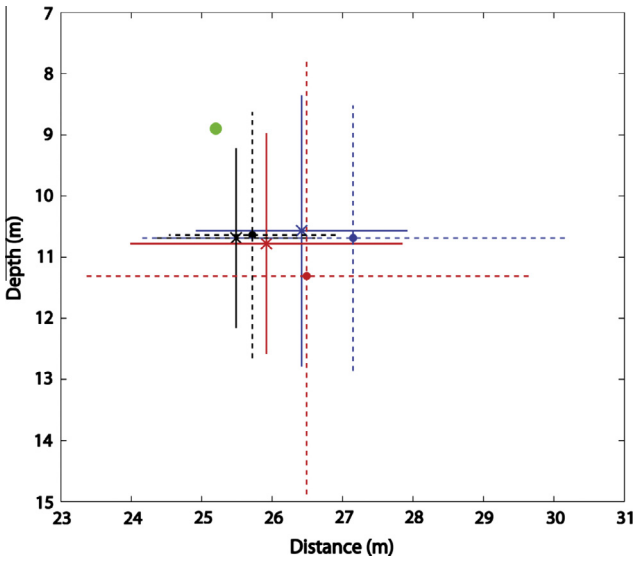

Fig. 8. Plots of the means and standard deviations of center of mass estimates based on 100 realizations of Gaussian noise additives (Eq. (6)). The green circle represents the true center of mass; the blue, red, and black denote the lateral, diagonal, and vertical positioning errors, respectively. The cross and the thick lines represent the final mean position of the realizations and one standard deviation for the 3% signal noise perturbations, whereas the circles and the broken lines mark the mean and standard deviation for the 10% signal noise case. The horizontal and vertical lines denote the lateral and vertical standard deviations. (For interpretation of the references to color in this figure legend, the reader is referred to the web version of this article.)

bias is therefore best assessed by directly comparing the spatial moments of the true and estimated concentration plumes.

4.2. Quantification of plume spatial moments

As mentioned earlier, the electrical conductivity images were back transformed to concentrations using the same equation applied in the forward transformation from concentration to conductivity when generating the test data. It is also important to note that inherent errors as a result of forward and inverse transformations between electrical conductivities and concentrations, encountered in practical applications, were not accounted for in the results presented here. The accuracies of the zeroth, first, and second spatial moments of the concentration plumes were then estimated from the images using Eq. (1). Given that differences in where the final positions of TIs converged in the preceding noise analysis were not significant, we report here only the results for the single realization of data noise associated with the images produced in Figs. 5 and 6.

The spatial moments estimated from the plume images generally degrade with increasing data noise, though all results are reasonably similar to the moments obtained directly from the true plume (Table 1). For the case of synthetic #1, the total mass (zeroth moment) was over-estimated by 0.6%, 0.6%, and 4.4% for the 0%, 3%, and 10% data errors, respectively. Relative errors in the estimated center of mass (first moment) for the 0%, 3%, and 10% data uncertainty cases were −1.0%, 0.6%, and 5.0% for the lateral position and −1.5%, −1.3%, and −9.6% for the vertical position. Relative errors in the estimated plume size (second moment) for the 0%, 3%, and 10% data errors were −3.5%, 9.7%, and 32.6% (lateral variance) and −3.4%, −21.9%, and 19.3% (vertical variance). These results indicate that estimates of the total solute mass and location of the plume are relatively robust to noise, though the overall size of the plume is more difficult to constrain accurately. In the case of synthetic #2, the estimation accuracy of the spatial moments also generally degraded with increasing data noise (Table 1), though the errors were slightly larger and patterns not always clear. For example, the relative error in the estimated center of mass in the lateral direction was −0.5, 0.6 and 4.0 for the 0%, 3%, and 10% data noise cases, which is consistent with what was observed for synthetic #1. The center of mass in the vertical direction, however, has a substantially higher relative error (9%) for the 0% data noise case than the 3% and 10% data noise cases with relative errors of −5.4% and −3.8%, respectively. Similarly, the lateral and vertical plume variance errors were 12.7%, 11.7%, and 3.3% (lateral variance) and −14.7%, −36.5%, and −45.0% (vertical variance), for the 0%, 3%, and 10% data uncertainties, respectively. These inconsistencies compared to case #1 are associated with the fact that the TIs used to generate the POD basis are conceptually inaccurate for representing the bimodal plume of synthetic #2, as was pointed out early in the context of the reconstruction of Fig. 6. A close inspection of Fig. 6j, r, and y, for example, reveal that the bottom portion of the bimodal plume (i.e., the second mode) was not fully reconstructed, which explains the relatively high errors in the quantified vertical plume variances for synthetic #2. Regardless of these observations, the overall magnitude of the observed moment errors is relatively modest given that the estimates are obtained using a non-invasive imaging technique.

We emphasize that the laterally central locations of the target plumes were deliberately chosen for maximum resistivity sensitivity. Therefore, we anticipate the resolution of the lateral center of mass to degrade as the target plume is shifted toward the lateral terminals within the domain as pointed out by Day-Lewis et al. (2007).

The literature suggests that the accuracy of the spatial moments estimated using the adaptive POD algorithm in this paper is generally consistent with or slightly better than past experiences achieved with geophysical tomography. Pidlisecky et al. (2011), for example, found percentage mass recovery errors in the range of 0% to −12%, center of mass errors in the range of 0–30% (lateral) and 2.7–7.5% (vertical), and spatial variance calibration errors of −10% to −80% (lateral) and −40% to −70% (vertical), though their experiment was a 2D synthetic study of cross-borehole ground-penetrating radar and therefore has substantially different resolution characteristics from the surface based resistivity surveys used in this paper. While direct comparisons across studies with different survey geometries, transport processes, and imaging methods are difficult, the value of the resistivity-based spatial moments estimated in this study can be directly compared to the moments estimated from direct sampling of the solute concentrations.

We simulate direct sampling of the solute plume in Synthetic #1 by placing synthetic boreholes at discrete locations along the cross-section, where for convenience we assume that the entire depth profile of concentration is sampled. It is clear from Fig. 9 that the estimation accuracy of plume moments from direct sampling is dependent on sampling coverage and the specific locations of the boreholes relative to the true plume. The moments estimated by direct sampling approach the true plume moments as the number of boreholes increases, stabilizing when approximately 12 boreholes are present or, equivalently, 0.12% of the image has been sampled. The estimate of the vertical center of mass is an exception which appears to retain a slight bias for the limited number of wells shown.

Using Fig. 9 to compare the center of mass estimates obtained from the resistivity surveys with no and 3% noise to those obtained by direct sampling indicates that the geophysically-based moments are more reliable than those obtained by direct sampling until at least 6–10 wells have been installed. Direct sampling almost always outperforms the resistivity surveys with 10% data noise, however, which demonstrates that the quality of the resistivity data is an important factor in determining its overall

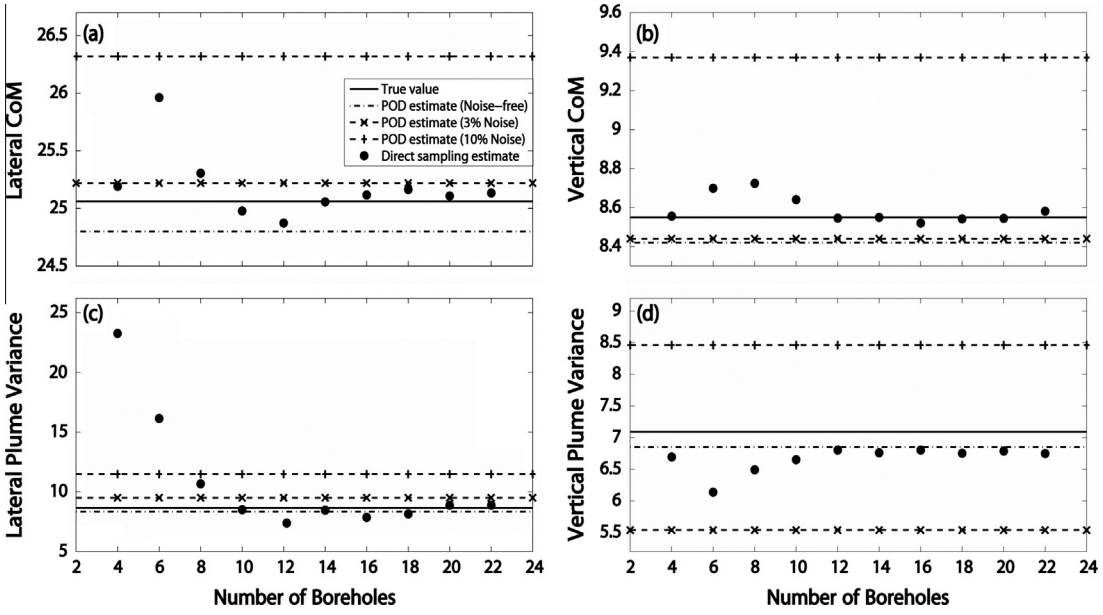

Fig. 9. Plots comparing the plume spatial moments estimated from resistivity imaging versus direct sampling approaches; upper imagines show results for the center of mass estimated in the lateral (a) and vertical (b) direction, whereas the lower images show results for the plume size in the lateral (c) and vertical (d) directions.

value. Similar conclusions can be made for the quality of estimates of the plume size (second moment) and mass (not shown). While the particulars of this comparison are dependent on the details of the specific situation studied, we suggest that these results do support the conclusion that POD-constrained resistivity images provide a promising alternative to extensive direct sampling for reasonably accurate estimation of the spatial moments of solute plumes.

5. Conclusions

An adaptive POD-based ERT strategy for inferring the spatial moments of subsurface solute plumes was presented. The proposed approach extends the POD inversion strategy introduced by Oware et al. (2013) to iteratively update the spatial location of the POD training images (TIs) (or equivalently the POD basis functions). The algorithm recursively refines the position of the TIs until their position is conditioned on the observed resistivity data. The approach was tested using two hypothetical transport scenarios: synthetic #1, which consists of a unimodal plume that is consistent with the transport model used to produce the POD TIs, and synthetic #2, where the target plume has two source locations that result in a bimodal plume that is inconsistent with the POD TIs.

The adaptive algorithm converged by shifting the TIs to a common region on the domain near the true plume regardless of TI starting position. Although the mean final position of the TIs inverted with 100 different realizations of data noise converged farther away from the center of mass of the true plume as the noise level of the resistivity data was increased, Oware et al. (2013) demonstrated that the TIs did not have to be precisely positioned at the center of mass of the true plume for the POD strategy to be successful. In all cases the final resistivity images provided reasonably accurate representations of the solute plume regardless of issues associated with data noise, the initial TI positioning, or conceptual inconsistencies between the target plume and simulations used to generate the TIs.

Estimates for the spatial moments of the plume based on the proposed imaging strategy were compared to those retrieved from the direct sampling of concentration values. Overall, the total mass and center of mass of the plumes could be accurately quantified by the resistivity results, but the spatial spread of the plume was more difficult to constrain. The estimation accuracy of the moments was found to deteriorate as the noise in the resistivity data increases. Spatial moment evaluations for synthetic #1 are better than the estimates for synthetic #2 due to the inaccurate basis functions applied to constrain the reconstruction of synthetic #2. We also found, however, that the data noise stabilized the inversion process in the case of synthetic #2. For low noise cases (i.e., the 0% and 3% noise cases in this study), the moments estimated from the resistivity images were found to outperform estimates based on direct concentration sampling until 6–10 multi-level sampling wells were installed. Although this particular number of wells is specific to our example, installing any number of multi-port sampling wells in field applications is not trivial given the time, labor, and cost involved in installing boreholes.

The POD algorithm appears particularly appealing due to its MOR capabilities. For instance, in this study, we achieved 97% truncation in the dimensionality of the original problem (i.e., 300 coefficients were estimated to reconstruct an image with 10,000 pixels). Reducing the number of parameters in an inverse problem may result in reductions in computational overhead and a possible improvement in the ill-posedness of the problem.

While our study illustrates a successful application of the adaptive POD-based imaging technique, there are a variety of issues that should be noted. First, the approach will not overcome fundamental sensitivity limitations of resistivity data. For example, if the training images are initially located beyond the influence of the resistivity data, then it will not be possible to shift their locations toward the location of the plume using our framework. Second, the POD basis is limited to capturing patterns representative of the conceptual model used to generate the TIs. Additional research is required to evaluate how this problem might be overcome using adaptive training data, supplementing the POD basis with additional patterns, or using geostatistical tools to capture additional spatial variability. Finally, we have not evaluated how the POD imaging technique or the estimated spatial moments of a plume may be affected by fluctuations in the background resistivity of the aquifer caused by geologic variability or associated uncertainties in the petrophysical relationship between concentration and bulk resistivity.

Despite these limitations, we conclude from this synthetic study that POD-based resistivity imaging provides a viable means for the inference of spatial moments of solute plumes in a noninvasive and cost-effective manner. We look forward to future efforts to undertake field-scale studies to evaluate the generalizability of our numerical findings to real-world settings.

Acknowledgement

We thank two anonymous reviewers and Ty Ferrè for their thoughtful reviews and suggestions that were used to improve this manuscript. This material is based upon work supported by the National Science Foundation under Grant No. EAR-1151294.

References

Archie, G.E., 1942. The electrical resistivity log as an aid in determining some reservoir characteristics. Trans. Am. Inst. Min. Metall. Pet. Eng. 146, 54–62.
Banks, H.T., Joyner, M.L., Wincheski, B., Winfree, W.P., 2000. Nondestructive evaluation using a reduced-order computational methodology. Inverse Prob. 16, 929–945.
Binley, A., Cassiani, G., Middleton, R., Winship, P., 2002. Vadose zone flow model parameterisation using cross-borehole radar and resistivity imaging. J. Hydrol. 267, 147–159.
Brewster, M.I., Annan, A.P., Greenhouse, J.P., Kueper, B.H., Olhoeft, G.R., Redman, J.D., Sander, K.A., 1995. Observed migration of a controlled DNAPL release by geophysical methods. Groundwater 33 (6), 977–987.
Castleman, K.R., 1996. Digital Image Processing. Prentice Hall, Inc., Upper Saddle River, NJ.
Day-Lewis, F.D., Chen, Y., Singha, K., 2007. Moment inference from tomograms. Geophys. Res. Lett. 34, http://dx.doi.org/10.1029/2007GL031621.
de Barros, F.P.J., Nowak, W., 2010. On the link between contaminant source release conditions and plume prediction uncertainty. J. Contam. Hydrol. 116, 24–34. http://dx.doi.org/10.1016/j.jconhyd.2010.05.004.
Dey, A., Morrison, H.F., 1979. Resistivity modeling for arbitrarily shaped two-dimensional Structures. Geophys. Prospect. 27 (1), 106–136. http://dx.doi.org/10.1111/j.1365-478.1979.tb00961.x.
Ellis, R.G., Oldenburg, D.W., 1994. Applied geophysical inversion. Geophys. J. Int. 116, 5–11.
Everett, L.G., 1980. Groundwater Monitoring. General Electric Company, Shenectady, N.Y..
Fernàndez-Garcia, D., Rajaram, H., Illangasekare, T.H., 2005. Assessment of the predictive capabilities of stochastic theories in a three-dimensional laboratory test aquifer: effective hydraulic conductivity and temporal moments of breakthrough curves. Water Resour. Res. 41, W04002, http://dx.doi.org/10.1029/2004WR003523.
Fowler, D.E., Moysey, S.M.J., 2011. Estimation of aquifer transport parameters from resistivity monitoring data within a coupled inversion framework. J. Hydrol. 409, 545–554. http://dx.doi.org/10.1016/j.jhydrol.2011.08.063.
Fox, L., 1979. Finite Differences and Singularities in Elliptic Problems: A Survey of Numerical Methods for Partial Differential Equations. Oxford Univ. Press, pp. 43–68.
Freyberg, D.L., 1986. A natural gradient experiment on solute transport in a sand aquifer: 2. Spatial moments and the advection and dispersion of nonreactive tracers. Water Resour. Res. 22 (13), 2031–2046. http://dx.doi.org/10.1029/WR022i013p02031.
Goltz, M.N., Roberts, P.V., 1987. Using the method of moments to analyze three-dimensional diffusion-limited solute transport from temporal and spatial perspectives. Water Resour. Res. 23, 1575–1585.
Hubbard, S.S., Chen, J., Peterson, J., Majer, E.L., Williams, K.H., Swift, D.J., Mailloux, B., Rubin, Y., 2001. Hydrological characterization of the South Oyster bacterial transport site using geophysical data. Water Resour. Res. 37, 2431–2456.
Keller, G.V., Frischknecht, F.C., 1966. Electrical Methods in Geophysical Prospecting. Per-gamon Press, New York.
Kemna, A., Vanderborght, J., Kulessa, B., Vereecken, H., 2002. Imaging and characterisation of subsurface solute transport using electrical resistivity tomography (ERT) and equivalent transport models. J. Hydrol. 267, 125–146.
Kunisch, K., Volkwein, S., 2003. Galerkin proper orthogonal decomposition for a general equation in fluid dynamics. SIAM J. Numer. Anal. 40 (2), 492–515.
LaBreque, D.J., Miletto, M., Daily, W., Ramirez, A., Owen, E., 1996. The effects of noise on Occam's inversion of resistivity tomography data. Geophysics 6 (2), 538–548.
Lane Jr., J.W., Day-Lewis, F.D., Versteeg, R.J., Casey, C.C., 2004. Object-based inversion of crosswell radar tomography data to monitor vegetable oil injection experiments. J. Environ. Eng. Geophys. 9, 63–77.
Lane Jr., J.W., Day-Lewis, F.D., Casey, C.C., 2006. Geophysical monitoring of field-scale vegetable oil injections for biostimulation. Ground Water 44 (3), 430–443. http://dx.doi.org/10.1111/j.1745-6584.2005.00134.x.
Lazarovitch, N., Warrick, A.W., Furman, A., Šimůnek, J., 2007. Subsurface water distribution from drip irrigation described by moment analyses. Vadose Zone J. 6 (1), 116–123.
LeBlanc, D.R., Garabedian, S.P., Hess, K.M., Gelhar, L.W., Quadri, R.D., Stollenwerk, K.G., Wood, W.W., 1991. Large-scale natural gradient tracer test in sand and gravel, Cape Cod, Massachusetts: 1. Experimental design and observed tracer movement. Water Resour. Res. 27 (5), 895–910.
Li, Y.-T., Bai, Z., Su, Y., 2009. A two-directional arnoldi process and its application to parametric model order reduction. J. Comput. Appl. Math. 226, 10–21. http://dx.doi.org/10.1016/j.cam.2008.05.059.
Loaiciga, H.A., Charbeneau, R.J., Everett, L.G., Fogg, G.E., Hobbs, B.F., Rouhani, S., 1992. Review of ground-water quality monitoring network design. J. Hydraul. Eng. 118, 11–37.
Milanfer, P., Karl, W.C., Willsky, A.S., 1996. A moment-based variational approach to tomographic reconstruction. IEEE Trans. Image Process. 5, 459–470.
Miller, E.L., Kilmer, M., Rappaport, C., 2000. A new shape-based method for object localization and characterization from scattered field data. IEEE Trans. Geosci. Remote Sens. 38, 1682–1696.
Moysey, S., Knight, R.J., 2004. Modeling the field-scale relationship between dielectric constant and water content in heterogeneous systems. Water Resour. Res. 40, W03510. http://dx.doi.org/10.1029/2003WR002589.
Moysey, S.M.J., Singha, K., Knight, R., 2005. A framework for inferring field-scale rock physics relationship through numerical simulation. Geophys. Res. Lett. 32, L083. http://dx.doi.org/10.1029/2004GL022152.
Muller, K., Vanderborght, J., Englert, A., Kemna, A., Huisman, J.A., Rings, J., Vereecken, H., 2010. Imaging and characterization of solute transport during two tracer tests in a shallow aquifer using electrical resistivity tomography and multilevel groundwater samplers. Water Resour. Res. 46, W03502.
Oware, E.K., Moysey, S.M.J., Khan, T., 2013. Physically based regularization of hydrogeophysical inverse problems for improved imaging of process-driven systems. Water Resour. Res. 49. http://dx.doi.org/10.1002/wrcr.20462.
Pidlisecky, A., Haber, E., Knight, R., 2007. RESINVM3D: A 3D resistivity inversion package. Geophysics 72 (2), H1–H10. http://dx.doi.org/10.1190/1.2402499.
Pidlisecky, A., Singha, K., Day-Lewis, F.D., 2011. A distribution-based parameterization for improved tomographic imaging of solute plumes. Geophys. J. Int. 187, 214–224. http://dx.doi.org/10.1111/j.1365-246X.2011.05131.x.
Pinnau, R., 2008. Model Reduction via Proper Orthogonal Decomposition. In: Schilder, W.H.A., van der Vorst, H. (Eds.), Model Order Reduction: Theory, Research Aspects and Applications. Springer, New York, pp. 96–109.
Rathinam, M., Petzold, L.R., 2004. A new look at Proper Orthogonal Decomposition. SIAM J. Numer. Anal. 41 (5), 1893–1925.
Rubin, Y., 2003. Applied Stochastic Hydrogeology. Oxford University Press, Oxford.
Singha, K., Gorelick, S.M., 2005. Saline tracer visualized with three-dimensional electrical resistivity tomography: field-scale spatial moment analysis. Water Resour. Res. 41, W05023. http://dx.doi.org/10.1029/2004WR003460.
Singha, K., Moysey, S.M., 2006. Accounting for spatially variable resolution in electrical resistivity tomography through field-scale rock physics relations. Geophysics 71 (4), A25–A28. http://dx.doi.org/10.1190/1.2209753.
Tikhonov, A.N., Arsenin, V.Y., 1977. Solutions of Ill-Posed Problems. John Wiley & Sons.
Winton, C., Pettway, J., Kelley, C.T., Howington, S., Eslinger, O.J., 2011. Application of Proper Orthogonal Decomposition (POD) to inverse problems in saturated groundwater flow. Adv. Water Resour. 34, 1519–1526. http://dx.doi.org/10.1016/j.advwatres.2011.09.007.
Xiong, Y., Furman, A., Wallach, R., 2011. Moment analysis description of wetting and redistribution plumes in wettable water-repellent soils. J. Hydrol. 422–423, 30–42.
Yao, Y., Meerbergen, K., 2013. Parametric model order reduction of damped mechanical systems via the block arnoldi process. Appl. Math. Lett. 26, 643–648. http://dx.doi.org/10.1016/j.aml.2013.01.006.
Ye, M., Khaleel, R., Yeh, T.-C.J., 2005. Stochastic analysis of moisture plume dynamics of a field injection experiment. Water Resour. Res. 41, W03013. http://dx.doi.org/10.1029/2004WR003735.
Yeh, T.-C.J., Ye, M., Khaleel, R., 2005. Estimation of effective unsaturated hydraulic conductivity tensor using spatial moments of observed moisture plume. Water Resour. Res. 41, W03014. http://dx.doi.org/10.1029/2004WR003736.